

Revisiting wideband pulsar timing measurements

Abhimanyu Susobhanan^{1,2*}, Avinash Kumar Paladi^{3,1}, Réka Desmecht^{4,1}, Amarnath^{1,5}, Manjari Bagchi^{6,7}, Manoneeta Chakraborty⁸, Shaswata Chowdhury⁶, Suruj Jyoti Das⁹, Debabrata Deb¹⁰, Shantanu Desai¹¹, Churchil Dwivedi¹², Himanshu Grover¹³, Jibin Jose⁸, Bhal Chandra Joshi^{14,13}, Shubham Kala⁶, Fazal Kareem¹⁵, Kuldeep Meena¹⁶, Sushovan Mondal^{6,7}, K Nobleson¹⁷, B Arul Pandian^{5,18}, Kaustubh Rai¹⁹, Adya Shukla¹³, Manpreet Singh²⁰, Aman Srivastava^{21,11}, Mayuresh Surnis¹⁹, Hemanga Tahbildar¹⁹, Keitaro Takahashi¹⁷, Pratik Tarafdar²², Kunjal Vara¹⁹, Vaishnavi Vyasraj¹¹, Zenia Zuraiq²³,

¹Max-Planck-Institut für Gravitationsphysik (Albert-Einstein-Institut), Liebniz Universität Hannover, Callinstraße 38, D-30167 Hannover, Germany

²School of Physics, Indian Institute of Science Education and Research Thiruvananthapuram, Maruthamala P.O., Thiruvananthapuram 695551, Kerala, India

³Joint Astronomy Programme, Department of Physics, Indian Institute of Science, C. V. Raman Avenue, Bengaluru 560012, Karnataka, India

⁴Vrije Universiteit Brussel, Pleinlaan 2, B-1050 Brussels, Belgium

⁵Raman Research Institute, Bengaluru 560080, Karnataka, India

⁶The Institute of Mathematical Sciences, C. I. T. Campus, Taramani, Chennai 600113, Tamil Nadu, India

⁷Homi Bhabha National Institute, Training School Complex, Anushakti Nagar, Mumbai 400094, Maharashtra, India

⁸Department of Astronomy, Astrophysics, and Space Engineering, Indian Institute of Technology Indore, Indore 453552, Madhya Pradesh, India

⁹Particle Theory and Cosmology Group, Center for Theoretical Physics of the Universe, Institute for Basic Science, Daejeon 34126, Korea

¹⁰Centre for Space Research, North-West University, Private Bag X6001, Potchefstroom 2520, South Africa

¹¹Department of Physics, Indian Institute of Technology Hyderabad, Kandi, Telangana 502284, India

¹²Astronomy and Astrophysics Division, Physical Research Laboratory, Thaltej Campus, Ahmedabad 380059, Gujarat, India

¹³Department of Physics, Indian Institute of Technology Roorkee, Roorkee 247667, Uttarakhand, India

¹⁴National Centre for Radio Astrophysics, Savitribhai Phule Pune University Campus, Pune 411007, Maharashtra, India

¹⁵Max-Planck-Institut für Radioastronomie, Auf dem Hügel 69, 53121 Bonn, Germany

¹⁶UM-DAE Centre for Excellence in Basic Sciences, University of Mumbai, Vidyawargi, Mumbai 400098, Maharashtra, India

¹⁷Faculty of Advanced Science and Technology, Kumamoto University, 2-39-1 Kurokami, Kumamoto 860-8555, Japan

¹⁸Department of Physics and Electronics, CHRIST (Deemed to be University), Bengaluru 560029, Karnataka, India

¹⁹Department of Physics, Indian Institute of Science Education and Research Bhopal, Bhopal 462066, Madhya Pradesh, India

²⁰Department of Physical Sciences, Indian Institute of Science Education and Research Mohali, Sector 81, SAS Nagar, Mohali 140306, Punjab, India

²¹Department of Physics, GLA University, Mathura 281406, Uttar Pradesh, India

²²INAF - Osservatorio Astronomico di Cagliari, via della Scienza 5, 09047 Selargius (CA), Italy

²³Department of Physics, Indian Institute of Science, C. V. Raman Avenue, Bengaluru 560012, Karnataka, India

Accepted XXX. Received YYY; in original form ZZZ

ABSTRACT

In the wideband paradigm of pulsar timing, the time of arrival of a pulsar pulse is measured simultaneously with the corresponding dispersion measure from a frequency-resolved integrated pulse profile. We present a new method for performing wideband measurements that rigorously accounts for measurement noise. We demonstrate this method using observations of PSR J2124–3358 made as part of the Indian Pulsar Timing Array experiment using the upgraded Giant Metre-wave Radio Telescope, and show that our method produces more realistic measurement uncertainty estimates compared to the existing wideband measurement method.

Key words: pulsars: general – methods: data analysis

1 INTRODUCTION

Pulsars are rotating neutron stars whose electromagnetic radiation appears as periodic pulses to a terrestrial observer (Lorimer & Kramer 2012). They are characterized by high rotational stability, acting as accurate celestial clocks. Pulsar timing is the technique of tracking

a pulsar’s rotation by measuring the times of arrival (TOAs) of its pulses (Hobbs et al. 2006). Pulsar timing is one of the most precise techniques in astronomy with a wide range of applications, from spacecraft navigation (Deng et al. 2013) to gravitational wave detection (Agazie et al. 2024).

Radio signals emitted by a pulsar are dispersed as they propagate through the ionized interstellar medium (ISM), introducing a delay that is proportional to the electron column density along the line of

* E-mail: abhimanyu.susobhanan@aei.mpg.de

sight and inversely proportional to the square of the radio frequency (Backer & Hellings 1986). The electron column density towards a pulsar, known as the dispersion measure (DM), varies stochastically as a function of time due to the dynamic nature of the ISM and the relative motion of the pulsar with respect to the Earth. In addition to the pulsar rotation and interstellar dispersion, the TOAs measured at a terrestrial observatory are influenced by several astrophysical phenomena, including geometric and relativistic delays due to the orbital motion of the pulsar and the Earth, passing gravitational waves, and instrumental delays and noise (Hobbs et al. 2006; Edwards et al. 2006; Damour & Deruelle 1986; Estabrook & Wahlquist 1975). Pulsar timing involves characterizing all of these effects to construct a predictive model for the TOAs.

A pulsar observation using a radio telescope generates an observing frequency-resolved radio light curve. This light curve is folded using the known rotational frequency of the pulsar to obtain an integrated pulse profile, which gives the pulsar intensity as a function of the pulse phase and the observing frequency. In conventional pulsar timing, also known as narrowband timing, a frequency-resolved integrated pulse profile spanning multiple frequency sub-bands covering the observed band-pass is produced, and a TOA is measured from each sub-band independently by cross-correlating it against a similarly frequency-resolved template profile (Taylor 1992). On the other hand, in the wideband timing paradigm, a single TOA along with a DM is measured from a frequency-resolved two-dimensional integrated pulse profile, also known as a portrait, by cross-correlating it against a two-dimensional template (Pennucci et al. 2014; Liu et al. 2014). Wideband timing can also be performed on combined datasets consisting of simultaneous multi-band observations (Paladi et al. 2024). The two-dimensional templates for wideband timing, also known as template portraits, are usually obtained using a principal component analysis-based method, described in Pennucci (2019). In general, a wideband timing measurement produces the TOA and DM estimates, their uncertainties, and their covariance, although it turns out that the measurement covariance can be made to vanish by adjusting the fiducial frequency at which the measurement is made; see Section 2. Consequently, wideband timing and noise analysis are done by incorporating both the TOA and the DM measurements (Alam et al. 2021; Susobhanan & van Haasteren 2025; Susobhanan 2025). Wideband timing provides two main advantages over narrowband timing — reduced data volumes and better handling of frequency-dependent profile variability (Hankins & Rickett 1986).

In this work, we present an improved method for wideband TOA and DM measurements, which provides better handling of the noise present in the observed portrait, thereby producing more realistic estimates of the measurement uncertainty. This paper is arranged as follows. In Section 2, we derive our new method for wideband measurements, starting from first principles. In Section 3, we demonstrate our method using a simulated example profile. In Section 4, we demonstrate our methods using data obtained as part of the Indian Pulsar Timing Array (InPTA) experiment (Joshi et al. 2018; Tarafdar et al. 2022; Rana et al. 2025). Finally, we summarize our results in Section 5.

2 REVISITING WIDEBAND MEASUREMENTS

We begin by writing down a model for the observed total intensity portrait as a function of the pulse phase ϕ and the observing frequency ν following Pennucci et al. (2014).

$$P(\phi, \nu) = b(\nu) + a(\nu)T(\nu, \phi - \varphi(\nu)) + n(\phi, \nu), \quad (1)$$

where $P(\phi, \nu)$ is the observed portrait, $T(\phi, \nu)$ is the template portrait, $b(\nu)$ is the baseline total intensity, $a(\nu)$ is the amplitude of the signal at each frequency, $\varphi(\nu)$ is a frequency-dependent phase shift, and $n(\phi, \nu)$ is a white noise process. The frequency dependence of $a(\nu)$ and $b(\nu)$ arises because of the pulsar's intrinsic emission spectrum (Maron et al. 2000), interstellar scintillation (Rickett 1970), and the shape of the telescope bandpass. The phase shift $\varphi(\nu)$ is given by

$$\varphi(\nu) = \varphi_0 - \kappa D \bar{F} \left(\nu^{-2} - \nu_{\text{ref}}^{-2} \right), \quad (2)$$

where φ_0 is the total phase shift due to achromatic effects, κ is the DM constant, D is the DM at the observing epoch, \bar{F} is the topocentric frequency of the pulsar at the observing epoch, and ν_{ref} is an arbitrary fiducial observing frequency. The phase shift φ_0 is related to the wideband TOA t_{arr} as

$$t_{\text{arr}} = t_{\text{obs}} + \bar{F}^{-1} \varphi_0, \quad (3)$$

where t_{obs} is the fiducial observation time, usually taken to be at the middle of the observation span. The noise term $n(\phi, \nu)$ arises due to radiometer noise, pulse jitter, radio frequency interference (RFI), etc.

In practice, the observed portrait is discrete, and equation (1) can be written in a discrete form as

$$P_{\alpha j} = b_{\alpha} + a_{\alpha} T(\nu_{\alpha}, \phi_j - \varphi_{\alpha}) + n_{\alpha j}, \quad (4)$$

where $\alpha \in \{1, \dots, N_{\text{chan}}\}$ represents the observing frequency channel, N_{chan} is the number of frequency channels, $j \in \{1, \dots, N_{\text{bin}}\}$ represents the pulse phase bin, N_{bin} is the number of phase bins, and $\varphi_{\alpha} = \varphi_0 - \kappa D \bar{F} (\nu_{\alpha}^{-2} - \nu_{\text{ref}}^{-2})$. Following Taylor (1992) and Pennucci et al. (2014), we compute the discrete Fourier transform of equation (4) along the phase index. Applying the Fourier shift theorem and discarding the zero-frequency baseline term, we obtain

$$\tilde{P}_{\alpha k} = a_{\alpha} \tilde{T}_{\alpha k} \exp[-2\pi i k \varphi_{\alpha}] + \tilde{n}_{\alpha k}, \quad (5)$$

where tilde ($\tilde{\cdot}$) represents the discrete Fourier transform, and $k \in \{1, \dots, N_{\text{bin}}\}$. Assuming $\tilde{n}_{\alpha k}$ to be an uncorrelated complex Gaussian process with an observing frequency-dependent variance σ_{α}^2 , we can write down a Fourier-domain log-likelihood function for the observed portrait:

$$\ln L = \sum_{\alpha=1}^{N_{\text{chan}}} \sum_{k=1}^{N_{\text{bin}}/2} \left[\frac{-|\tilde{P}_{\alpha k} - a_{\alpha} \tilde{T}_{\alpha k} \exp[-2\pi i k \varphi_{\alpha}]|^2}{\sigma_{\alpha}^2} - \ln[\pi \sigma_{\alpha}^2] \right] - \sum_{\alpha=1}^{N_{\text{chan}}} \left[\sigma_{\alpha}^{-2} \left(U_{\alpha} + a_{\alpha}^2 V_{\alpha} - 2a_{\alpha} W_{\alpha} \right) + \frac{N_{\text{bin}}}{2} \ln[\pi \sigma_{\alpha}^2] \right]. \quad (6)$$

We only consider Fourier frequencies up to $N_{\text{bin}}/2$ in the summation because both $P_{\alpha j}$ and $T_{\alpha j}$ are real-valued. The quantities U_{α} , V_{α} , and W_{α} are real-valued and are defined as

$$U_{\alpha} = \sum_{k=1}^{N_{\text{bin}}/2} |\tilde{P}_{\alpha k}|^2, \quad (7a)$$

$$V_{\alpha} = \sum_{k=1}^{N_{\text{bin}}/2} |\tilde{T}_{\alpha k}|^2, \quad (7b)$$

$$W_{\alpha} = \sum_{k=1}^{N_{\text{bin}}/2} \Re \left[\tilde{P}_{\alpha k} \tilde{T}_{\alpha k}^* \exp[2\pi i k \varphi_{\alpha}] \right]. \quad (7c)$$

Here, W_{α} is a function of φ_0 , D , and ν_{ref} , whereas U_{α} and V_{α} only depend on the data and the template portraits, respectively.

$\ln L$ is a function of the parameters of interest φ_0 and D , the nuisance parameters a_{α} and σ_{α} , and the arbitrary constant ν_{ref} . Pennucci

et al. (2014) removes the a_α dependence by maximizing equation (6) over those parameters, and fixes ν_{ref} by demanding that the measurement covariance between φ_0 and D vanish. Multiple methods have been employed to estimate the noise standard deviation σ_α . This includes using the variance within a window around the profile's minimum, assuming it lies in the off-pulse region, or estimating the variance based on the highest harmonics in the discrete Fourier transform $\tilde{P}_{\alpha k}$ (Pennucci et al. 2014). The latter method is implemented in `PulsePortraiture`. Unfortunately, these approaches do not always provide reliable noise estimates: for example, the former method fails for pulsars with large duty cycles and the latter fails when the profile signal-to-noise ratio is sufficiently high, making even the higher harmonics dominated by the signal. The latter failure mode occurs when (a) the pulsar is bright, (b) the telescope has a large collecting area, and/or (c) the pulsar is observed for a long duration.

To overcome this limitation, we explore a Bayesian approach to do away with the nuisance parameters. The Bayes' theorem in this context can be written as

$$\begin{aligned} p[\varphi_0, D, \mathbf{a}, \sigma | P, T] &= L[P | \varphi_0, D, \mathbf{a}, \sigma; T] \\ &\Pi[\varphi_0] \Pi[D] \Pi[\mathbf{a}] \Pi[\sigma] / Z[P|T], \end{aligned} \quad (8)$$

where p denotes the posterior distribution, the likelihood L is given by equation (6), Π denotes the prior distributions, Z is the Bayesian evidence, and \mathbf{a} and σ represent the collection of a_α and σ_α parameters respectively. We can marginalize equation (8) analytically over a_α and σ_α by imposing the appropriate conjugate priors on those parameters. It turns out, from equation (6), that the conjugate prior on a_α is a Gaussian distribution and the conjugate prior on σ_α is an inverse-gamma distribution, whose probability density function is given by

$$\Pi(\sigma_\alpha; p, q) = \frac{q^p}{\Gamma(p)} \sigma_\alpha^{-p-1} \exp(-\sigma_\alpha/x).$$

Since we do not have any prior information on a_α or σ_α except that the latter should be positive, we choose $\Pi[a_\alpha]$ to be a Gaussian distribution with infinite variance (same as an infinitely wide uniform distribution), i.e., $\Pi[a_\alpha] \propto 1$. Further, we choose an improper log-uniform prior for σ_α , corresponding to $\Pi[\sigma_\alpha] \propto \sigma_\alpha^{-1}$, which is the same as the limiting case of an inverse-gamma distribution with $p, q \rightarrow 0$ (this is the same as the Jeffreys' prior; Jeffreys (1946)).

Marginalizing equation (8) over the a_α and σ_α using the above-mentioned prior distributions, we obtain

$$p[\varphi_0, D | P, T] = \Pi[\varphi_0] \Pi[D] \Lambda[P | \varphi_0, D], \quad (9)$$

where the marginalized log-likelihood can be written, up to an additive constant, as

$$\ln \Lambda = \frac{-(N_{\text{bin}} - 1)}{2} \sum_\alpha \ln \left(U_\alpha - \frac{W_\alpha^2}{V_\alpha} \right). \quad (10)$$

A detailed derivation of equation (10) is provided in Appendix A.

We note in passing that an alternative to marginalization is the profile likelihood approach (Herold et al. 2025), where the likelihood function is *maximized* over the nuisance parameters. This approach yields an expression that is very similar to equation (10):

$$\ln \hat{\mathcal{L}} = \frac{-N_{\text{bin}}}{2} \sum_\alpha \ln \left(U_\alpha - \frac{W_\alpha^2}{V_\alpha} \right); \quad (11)$$

see Appendix B for a detailed derivation. A careful inspection of these expressions reveals that both equations (10) and (11) provide the same maximum-likelihood estimate, but equation (10) provides slightly broader and more conservative measurement uncertainty estimates.

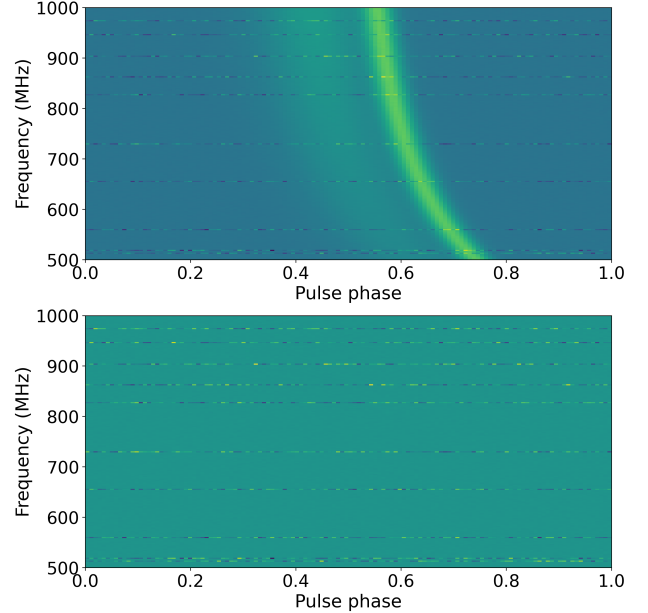


Figure 1. The top plot shows the simulated pulse portrait based on the analytic two-peaked template given in equation (12), also containing white noise in each frequency channel. Ten randomly selected channels have noise injections with a significantly higher amplitude, simulating RFI, and these are visible in the plot as horizontal stripes. The bottom plot shows the post-fit residuals of the portrait, which are determined by subtracting the best-fitting model from the simulated data. The residuals show only noise, indicating a successful fit.

Note that we use equation (10) exclusively in the remainder of this paper, and equation (11) is shown only for comparison.

Since the fiducial frequency ν_{ref} is arbitrary, it is usually chosen such that the measurement covariance between φ_0 and D vanishes, so that they can be treated as independent measurements, in turn simplifying and reducing the computational cost of wideband timing and noise analysis (Alam et al. 2021; Susobhanan & van Haasteren 2025). This is achieved in Pennucci et al. (2014) using a Hessian-based analytic estimate of the measurement covariance, by setting the second derivative $\frac{\partial^2 \ln L}{\partial \varphi_0 \partial D}$ to zero. This choice of the fiducial frequency for our noise-marginalized likelihood, denoted $\bar{\nu}_{\text{ref}}$, is derived in Appendix C. It can be seen from Appendix C that (a) the $\bar{\nu}_{\text{ref}}$ depends on the observed portrait on each epoch, and therefore is different for each epoch, and (b) the $\bar{\nu}_{\text{ref}}$ estimate is derived assuming a Gaussian posterior distribution, and may not be accurate when the posterior is significantly non-Gaussian, e.g., in the presence of loud RFI. The measurement uncertainties in φ_0 and D can also be estimated with the help of the Hessian, and these computations are also described in Appendix C.

3 A SIMULATED EXAMPLE

We now turn to an example to showcase our method using a simulated portrait. We assume a frequency-dependent two-peaked template portrait of the form

$$T(\phi, \nu) = \frac{3}{5} \text{vm}[\phi; \pi, 60] + \frac{2}{5} \left(\frac{\nu}{400 \text{ MHz}} \right) \text{vm} \left[\phi; \frac{3\pi}{4}, 5 \right], \quad (12)$$

where $\text{vm}[\phi; \mu, \chi]$ is the von Mises function given by

$$\text{vm}[\phi; \mu, \chi] = \frac{\exp(\chi \cos(\phi - \mu))}{2\pi I_0(\chi)}.$$

We simulate an observed portrait using equation (4) with $b(\nu) = 0.2$, $a(\nu) = 2$, $\varphi_0 = 0.1$, $D = 0.15 \text{ pc/cm}^3$, $\nu_{\text{ref}} = 750 \text{ MHz}$, $\bar{F} = 100 \text{ Hz}$, $N_{\text{bin}} = 128$, and $N_{\text{chan}} = 256$ for observing frequencies between 500–1000 MHz. We inject white noise realizations with a standard deviation $\sigma_\alpha = 0.025$ in every frequency channel, except for 10 randomly selected channels where we use $\sigma_\alpha = 0.25$ to simulate RFI. The resulting simulated portrait is shown in Figure 1.

We estimate φ_0 and D from this simulated template using the amplitude and noise-marginalized likelihood function of equation (10). Assuming broad uniform priors for φ_0 and D , we draw samples from the posterior distribution (equation 9) using the MultiNest nested sampling algorithm (Feroz et al. 2009), implemented in the `nestle` package (Barbary 2021). The posterior distribution $p[\varphi_0, D | P, T]$ at a fiducial frequency $\bar{\nu}_{\text{ref}}$ estimated based on Appendix C is plotted in Figure 2. The portrait residuals, obtained by subtracting the best-fit model from the data portrait in this case, are plotted in the lower panel of Figure 1. We find that the injected φ_0 and D values are reliably estimated, and that the residuals in each frequency channel are white.

We now proceed to ascertain the accuracy of the $\bar{\nu}_{\text{ref}}$ obtained in Appendix C. For this purpose, we estimate φ_0 and D using 101 uniformly separated values of ν_{ref} in the 400–1100 MHz range using the noise-marginalized likelihood of equation (10) using nested sampling. We find that the estimated φ_0 and D values are consistent with the injected values for every value of ν_{ref} , as expected¹. We plot the Pearson correlation coefficient between φ_0 and D as a function of ν_{ref} in Figure 3. We find that the correlation becomes approximately zero at $\nu_{\text{ref}} = \bar{\nu}_{\text{ref}}$, although a tiny correlation remains even at this ν_{ref} value². We also plot the determinant of the covariance matrix, which is a measure of the total uncertainty in the wideband measurement, as a function of ν_{ref} , in Figure 3. We find that this determinant value remains independent of ν_{ref} up to numerical precision, indicating that the overall measurement precision is not affected by the choice of ν_{ref} .

4 DEMONSTRATION USING InPTA OBSERVATIONS OF PSR J2124–3358

We now proceed to demonstrate our new wideband measurement method using frequency-resolved integrated pulse profiles of PSR J2124–3358 and compare it against the wideband measurement method of Pennucci et al. (2014). PSR J2124–3358 is a bright, nearby, and isolated millisecond pulsar with a rotational period $P_s \sim 4.93 \text{ ms}$, located at a distance of around 400 pc. It was discovered using the Parkes 64-m Radio Telescope in the Parkes 436 MHz survey of the southern sky (Bailes et al. 1997). Its stable, precisely timed pulses make it an important target for pulsar timing array (PTA) experiments (e.g. Rana et al. 2025).

The data used in this section include integrated pulse profiles obtained from observations done using the upgraded Giant Metre-wave Radio Telescope (uGMRT; Gupta et al. 2017) as part of the InPTA experiment (Joshi et al. 2018) during observation cycles 37–48 (MJD 58781–60896) in the 300–500 MHz band (Band 3). TOAs derived

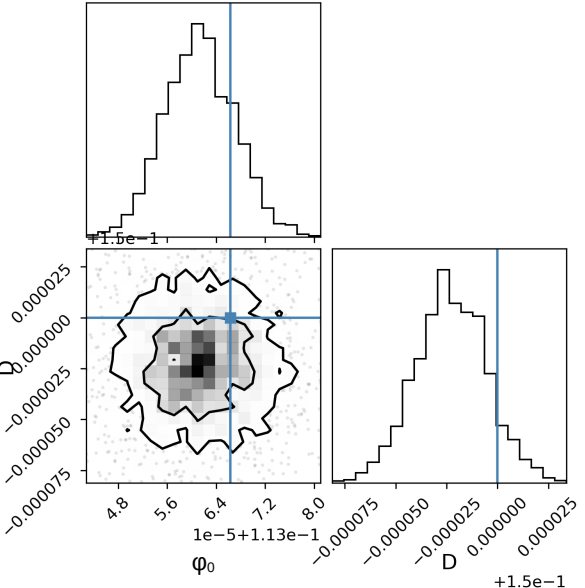


Figure 2. The posterior distribution obtained from the simulated portrait described in Section 3. This analysis was done using a fiducial frequency value such that the measurement covariance between the two parameters vanishes (i.e., $\bar{\nu}_{\text{ref}}$), as described in Appendix C. The blue lines represent the injected values shifted according to the $\bar{\nu}_{\text{ref}}$. This corresponds to $\varphi_{0;\text{inj}} - \kappa D F(v_{\text{ref};\text{inj}}^2 - \bar{\nu}_{\text{ref}}^2)$ for the φ_0 measurement whereas the D measurement is expected to be consistent with D_{inj} , where the label ‘inj’ represents the injected value. The simulated portrait and the post-fit residuals are plotted in Figure 1. The estimated parameters are consistent with the injected values up to a shift described above. The contours represent 68% and 95% credible intervals.

from subsets of this data were included in the first and second data releases of the InPTA (Tarafdar et al. 2022; Rana et al. 2025); however, the epochs 60426–60896 have not been published elsewhere. The observation and data reduction procedures used to obtain this dataset are described in Susobhanan et al. (2021), Tarafdar et al. (2022), and Rana et al. (2025). We have excluded observing epochs significantly affected by RFI from this analysis.

The wideband measurement technique described in Pennucci et al. (2014) and implemented in the `PulsePortraiture` package is henceforth referred to as the standard timing technique. In the standard technique, the noise parameters σ_α are estimated by considering the mean of the last 25%³ of the Fourier bins in the power spectrum computed from $\tilde{P}_{\alpha k}$. We have implemented the amplitude and noise-marginalized likelihood given in equation (10) in `PulsePortraiture`, and this is referred to as MLAN⁴ hereafter.

We applied these two methods to the frequency-resolved integrated pulse profiles of PSR J2124–3358 to measure the wideband TOAs and DMs. The wideband DM time series obtained using the two methods are shown in Figure 4. We find that the DM estimates obtained using the two methods are not always identical, and there are

¹ The measured φ_0 value depends on ν_{ref} . We deem the measured φ_0 value to be consistent with the injected value if $|\varphi_0^{\text{meas}} - \varphi_0^{\text{inj}} - \kappa D F(\nu_{\text{ref}}^{\text{meas}} - \nu_{\text{ref}}^{\text{inj}})|$ is less than the measurement uncertainty of φ_0 , where the superscripts ‘meas’ and ‘inj’ indicate the measured and injected values. On the other hand, the measured D value should be independent of ν_{ref} .

² A similar observation was also made by Pennucci et al. (2014)

³ This fraction (25%) can be adjusted while running `PulsePortraiture`. Unfortunately, there is no rigorous procedure to determine the optimal value of this fraction, so we have persisted with the default value used in `PulsePortraiture`. Further, this value has been used in previous InPTA wideband analyses (Nobleson et al. 2022; Tarafdar et al. 2022).

⁴ Marginalized Likelihood over Amplitude and Noise

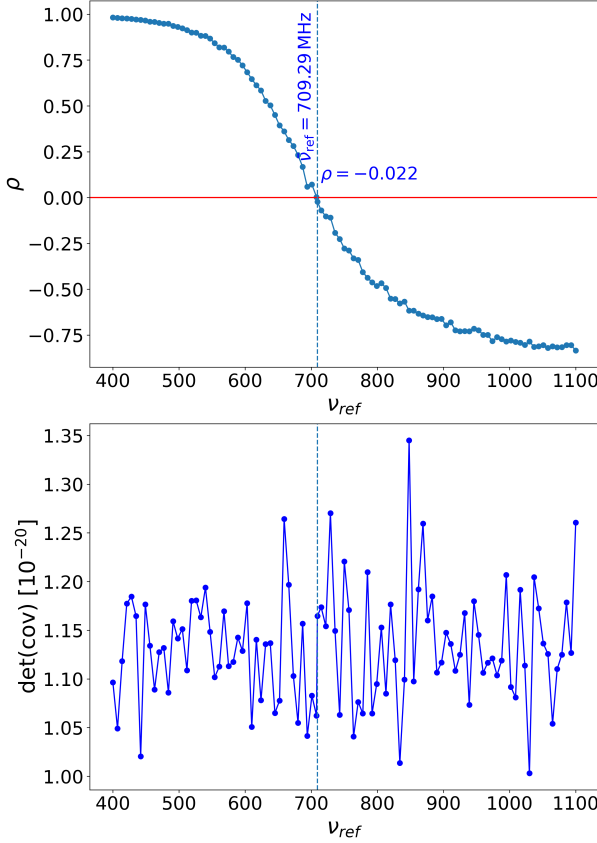


Figure 3. The top plot shows the measurement correlation ρ between φ_0 and D as a function of ν_{ref} . The $\bar{\nu}_{\text{ref}}$ value computed based on Appendix C is indicated using a vertical dotted line, and the corresponding correlation estimated from posterior samples is indicated using a horizontal red line. The correlation at $\bar{\nu}_{\text{ref}}$ is very close to zero. The bottom plot shows the determinant of the covariance matrix between φ_0 and D as a function of ν_{ref} . This determinant is a measure of the total measurement uncertainty, and does not show any significant variation as a function of ν_{ref} except for random scatter. The scatter seen in the two plots is due to the numerical error from using a finite number of posterior samples.

a few epochs where the measurements are inconsistent. Nevertheless, the DM measurements are consistent on the majority of epochs.

A comparison of the TOA and DM measurement uncertainties obtained using the two methods is shown in Figure 5. We find that the measurement uncertainties obtained with the MLAN method are consistently greater than those obtained with the standard method. In particular, the discrepancy in uncertainties is larger for high-S/N epochs. We argue that this is because the σ_α estimates used in the standard method, computed from higher harmonics in the power spectrum derived from $\tilde{P}_{\alpha k}$, are inaccurate, especially when the S/N is high, where even the higher Fourier bins in the power spectrum will be dominated by signal. On the other hand, the MLAN method provides a rigorous treatment of the noise in each frequency channel since the σ_α parameters are analytically marginalized.

We performed timing analysis on the two sets of TOAs using the PINT package (Luo et al. 2021; Susobhanan et al. 2024). We start our initial timing analysis using the pulsar ephemeris published in Rana et al. (2025). The timing model includes pulsar spin-down parameterized by the frequency F0 and the frequency derivative F1, secular DM evolution parameterized by an average DM and two derivatives (DM1, DM2), and astrometric delays with the sky location (RA,

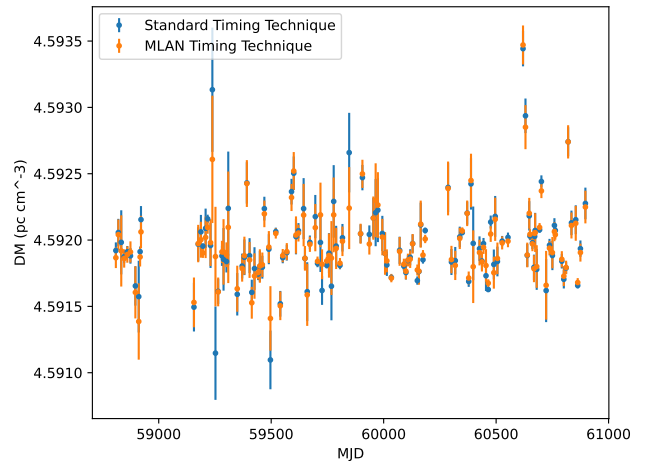


Figure 4. DM time series for PSR J2124-3358 obtained using the standard and MLAN measurement methods. The measurements are consistent but not identical, except for a few epochs where there is a significant difference between the two methods.

DEC) as free parameters. These are the same parameters that are fitted in the InPTA Data Release 2 narrowband dataset (Rana et al. 2025). Proper motion and parallax are not fitted, but fixed to values taken from the European Pulsar Timing Array Data Release 2 (Antoniadis et al. 2023). The TOA and DM residuals for standard and MLAN methods are plotted in Figure 6.

After the initial timing, we performed single-pulsar noise analysis (SPNA) using a linearized timing model following the method described in Susobhanan & van Haasteren (2025). We recall that the Bayes' theorem for SPNA is given by

$$\mathcal{P}[\Theta|\mathfrak{D}, \mathfrak{M}] = \mathcal{L}[\mathfrak{D}|\Theta, \mathfrak{M}] \Pr[\Theta|\mathfrak{M}] / \mathcal{Z}[\mathfrak{D}|\mathfrak{M}], \quad (13)$$

where \mathcal{P} , \mathcal{L} , \Pr , and \mathcal{Z} represent the posterior distribution, the likelihood function, the prior distribution, and the Bayesian evidence, respectively, of the SPNA. Further, \mathfrak{D} represents the wideband TOA and DM measurements, \mathfrak{M} represents the linearized timing and noise model, and Θ represents the collection of the linearized timing and noise model parameters. These are not to be confused with the objects appearing in equations (8) and (9), which provide the Bayes theorem in the context of a single wideband measurement. The SPNA likelihood \mathcal{L} is given by

$$\mathcal{L} = -\frac{1}{2} \mathbf{y}^T \mathbf{C}^{-1} \mathbf{y} - \frac{1}{2} \ln \det[2\pi \mathbf{C}] \quad (14)$$

where \mathbf{y} is a vector containing the TOA and DM residuals obtained from initial timing, \mathbf{C} is a covariance matrix usually expressed in a reduced-rank form $\mathbf{C} = \mathbf{N} + \mathbf{M}\Phi\mathbf{M}^T$, \mathbf{N} is a diagonal matrix containing modified TOA and DM measurement uncertainties, \mathbf{M} is a design matrix representing the linearized timing and noise model, and Φ is a prior covariance matrix for the amplitudes associated with the signals represented in \mathbf{M} .

We implemented the posterior distribution given in equation (13) with the help of PINT. We model inaccuracies in TOA measurement uncertainties and pulse jitter using an EFAC (error factor) and an EQUAD (error added in quadrature) (Kikunaga et al. 2024). Similarly, inaccuracies in DM measurement uncertainties are modeled using a DMEFAC. We model stochastic DM variations and the achromatic red noise (due to rotational irregularities and gravitational wave background; Agazie et al. (2024)) as Fourier series Gaussian

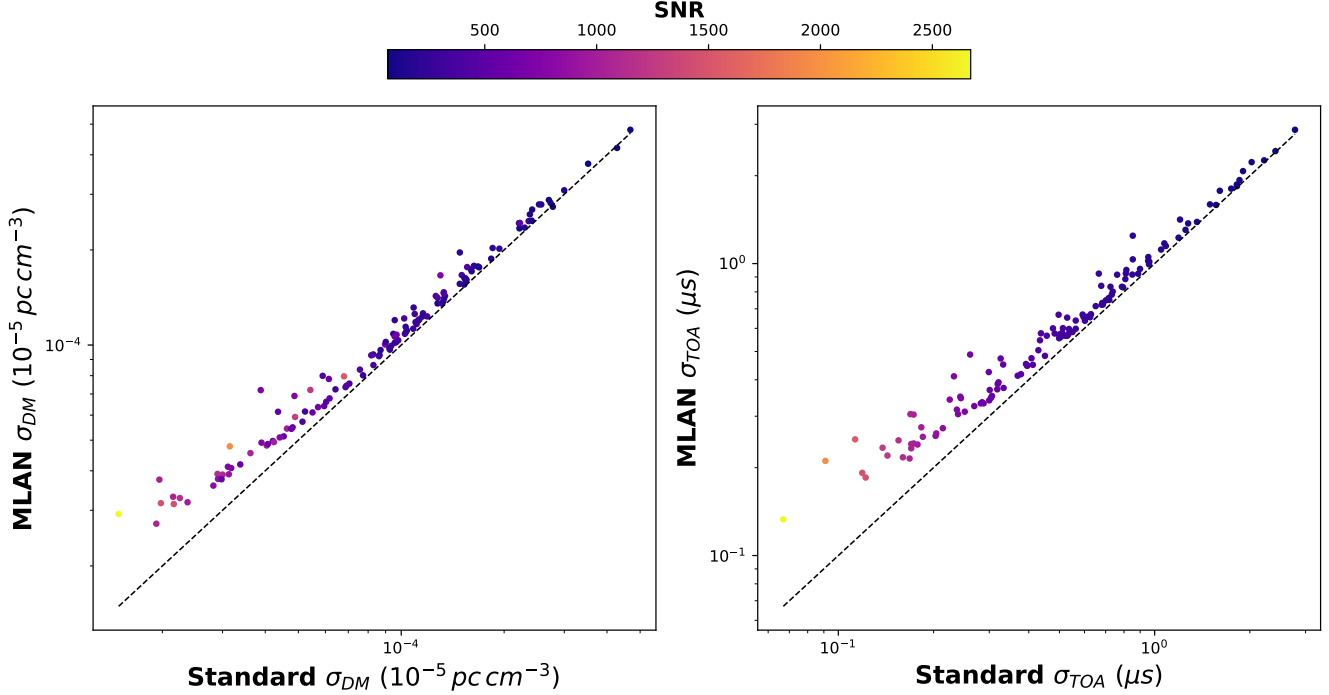


Figure 5. Comparison of TOA and DM measurement uncertainties obtained using the standard and MLAN methods. The S/N at each epoch is represented as the color of each point. The MLAN uncertainties are consistently higher than their standard method counterparts. This is most prominent in high-S/N epochs.

processes with power-law spectra. We use 50 linearly spaced frequency bins each for these Gaussian process models with a fundamental frequency $f_1 = T_{\text{span}}^{-1}$ where $T_{\text{span}} = 2087.5$ days. Following [van Haasteren & Vallisneri \(2014\)](#), we also include four logarithmically spaced frequency bins below f_1 to better capture the lower frequency components of the spin noise and DM noise (at $f_1/2$, $f_1/4$, $f_1/8$, and $f_1/16$). We perform parameter estimation on the wideband measurements using the above-mentioned model with the help of the `nautilus` package, which implements a neural network-boosted importance nested sampling algorithm ([Lange 2023](#)). We perform this analysis on wideband measurements obtained using both the standard and MLAN methods.

The posterior distributions obtained from this exercise are plotted in Figure 7. We find that the DMEFAC estimated from the MLAN measurements is lower than that estimated from the standard measurements. Similarly, the EFAC and the DM noise amplitude are slightly lower in the case of MLAN. On the other hand, EQUAD estimates are consistent between the standard and MLAN measurements, although the posterior distributions are not identical. Finally, achromatic red noise is not detected in this pulsar, and the posterior distributions are visually identical for both standard and MLAN measurements. These results are consistent with the standard method underestimating measurement uncertainties as seen in Figure 5, i.e., the MLAN method provides more realistic measurement uncertainty estimates than the standard method.

5 SUMMARY AND DISCUSSION

We derived a new method for performing wideband TOA and DM measurements from frequency-resolved integrated pulse profiles of a pulsar following a Bayesian approach. Our method, compared to the widely used wideband measurement method of [Pennucci et al. \(2014\)](#), features a more rigorous treatment of noise in each frequency channel of the profile, leading to more realistic TOA and DM measurement uncertainty estimates. Our method, similar to [Pennucci et al. \(2014\)](#), allows one to make *independent* TOA and DM measurements by choosing an appropriate fiducial observing frequency. We demonstrated our method using a simulated profile and showed that (a) it accurately recovers the injected parameter values, and (b) the fiducial observing frequency selection procedure is effective in removing the TOA-DM measurement covariance. We applied our method to the InPTA data of PSR J2124–3318, and compared its performance against the method of [Pennucci et al. \(2014\)](#). We showed that the TOA and DM measurement uncertainty estimates obtained using our method are indeed more realistic than those obtained using [Pennucci et al. \(2014\)](#). This is crucial for achieving a robust detection of nanohertz gravitational waves using the wideband timing method, since imprecise white noise estimates can lead to biases in pulsar timing array inference ([Antoniadis et al. 2024](#)).

In the coming years and decades, as the PTA datasets grow, the wideband technique will be crucial for ensuring that the computational cost of performing PTA analysis remains manageable. This work is a crucial stepping stone towards ensuring the reliability of the wideband timing method, so that it can be applied to high-precision timing experiments like pulsar timing arrays. We plan to apply our

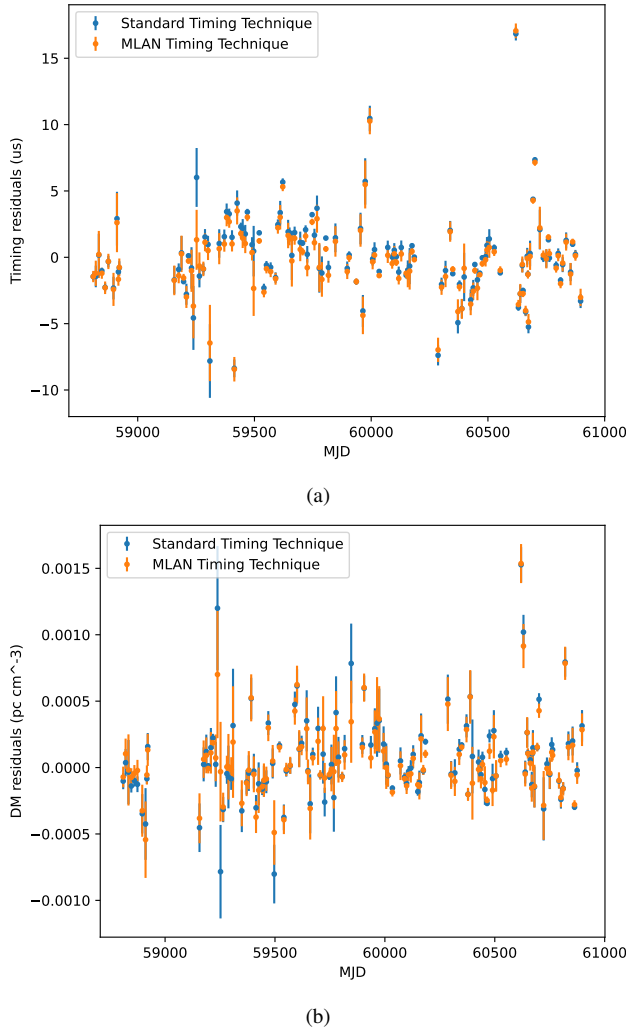


Figure 6. The TOA and DM residuals for PSR J2124–3358 derived from preliminary timing of the wideband measurements done using the standard and MLAN methods. The (b) panel of this plot looks similar to the DM measurements shown in Figure 4 because we have only fit a linear function to model the DM during preliminary timing, so the short-timescale DM variations are still present.

method to the full InPTA dataset in the near future as part of the second InPTA wideband data release.

ACKNOWLEDGMENTS

We thank the staff of the GMRT who made our observations possible. GMRT is run by the National Centre for Radio Astrophysics of the Tata Institute of Fundamental Research. SJD is supported by IBS under the project code IBS-R018-D1. SD is supported by SERB grant MTR/2023/000384. BCJ acknowledges the support from Raja Ramanna Chair fellowship of the Department of Atomic Energy, Government of India (RRC – Track I Grant 3/3401 Atomic Energy Research 00 004 Research and Development 27 02 31 1002//2/2023/RRC/R&D-II/13886 and 1002/2/2023/RRC/R&D-II/14369). KR is supported by UGC JRF fellowship. AdS is supported by UGC JRF fellowship HT is supported by DST INSPIRE Fellowship, INSPIRE code IF210656. KT is partially supported by JSPS KAKENHI Grant Numbers 20H00180, 21H01130,

21H04467, and 24H01813, and Bilateral Joint Research Projects of JSPS (120237710). KV is supported by CSIR JRF Fellowship. ZZ is supported by the Prime Minister’s Research Fellows scheme, Ref. No. TF/PMRF-22-7307.

SOFTWARE

PulsePortraiture (Pennucci et al. 2014; Pennucci 2019), PINT (Luo et al. 2021); Susobhanan et al. (2024), nestle (Barbary 2021), nautilus (Lange 2023), corner (Foreman-Mackey 2016), numpy (Harris et al. 2020), scipy (Virtanen et al. 2020), matplotlib (Hunter 2007)

DATA AVAILABILITY

The wideband TOAs and the ephemeris for PSR J2124–3358 are included as supplementary material.

REFERENCES

Agazie G., et al., 2024, *ApJ*, **966**, 105
 Alam M. F., Arzoumanian Z., Baker P. T., Blumer H., Bohler K. E., et al., 2021, *The Astrophysical Journal*, **252**, 5
 Antoniadis J., Babak S., Bak Nielsen A.-S., Bassa C. G., Berthureau A., et al., 2023, *A&A*, **678**, A48
 Antoniadis J., Arumugam P., Arumugam S., Babak S., Bagchi M., et al., 2024, *A&A*, **685**, A94
 Backer D. C., Hellings R. W., 1986, *Annual Review of Astronomy and Astrophysics*, **24**, 537
 Bailes M., et al., 1997, *ApJ*, **481**, 386
 Barbary K., 2021, nestle: Nested sampling algorithms for evaluating Bayesian evidence, *Astrophysics Source Code Library*, record ascl:2103.022 (ascl:2103.022)
 Damour T., Deruelle N., 1986, *Annales de L’Institut Henri Poincaré Section (A) Physique Théorique*, **44**, 263
 Deng X. P., et al., 2013, *Advances in Space Research*, **52**, 1602
 Edwards R. T., Hobbs G. B., Manchester R. N., 2006, *Monthly Notices of the Royal Astronomical Society*, **372**, 1549
 Estabrook F. B., Wahlquist H. D., 1975, *General Relativity and Gravitation*, **6**, 439
 Feroz F., Hobson M. P., Bridges M., 2009, *MNRAS*, **398**, 1601
 Foreman-Mackey D., 2016, *The Journal of Open Source Software*, **1**, 24
 Gupta Y., et al., 2017, *Current Science*, **113**, 707
 Hankins T. H., Rickett B. J., 1986, *The Astrophysical Journal*, **311**, 684
 Harris C. R., et al., 2020, *Nature*, **585**, 357
 Herold L., Ferreira E. G. M., Heinrich L., 2025, *Physical Review D*, **111**, 083504
 Hobbs G. B., Edwards R. T., Manchester R. N., 2006, *Monthly Notices of the Royal Astronomical Society*, **369**, 655
 Hunter J. D., 2007, *Computing in Science & Engineering*, **9**, 90
 Jeffreys H., 1946, *Proceedings of the Royal Society of London Series A*, **186**, 453
 Joshi B. C., et al., 2018, *Journal of Astrophysics and Astronomy*, **39**, 51
 Kikunaga T., et al., 2024, *Publ. Astron. Soc. Australia*, **41**, e036
 Lange J. U., 2023, *Monthly Notices of the Royal Astronomical Society*, **525**, 3181
 Liu K., et al., 2014, *Monthly Notices of the Royal Astronomical Society*, **443**, 3752
 Lorimer D. R., Kramer M., 2012, *Handbook of Pulsar Astronomy*. Cambridge University Press
 Luo J., Ransom S., Demorest P., Ray P. S., Archibald A., et al., 2021, *The Astrophysical Journal*, **911**, 45
 Maron O., Kijak J., Kramer M., Wielebinski R., 2000, *Astronomy and Astrophysics Supplement Series*, **147**, 195

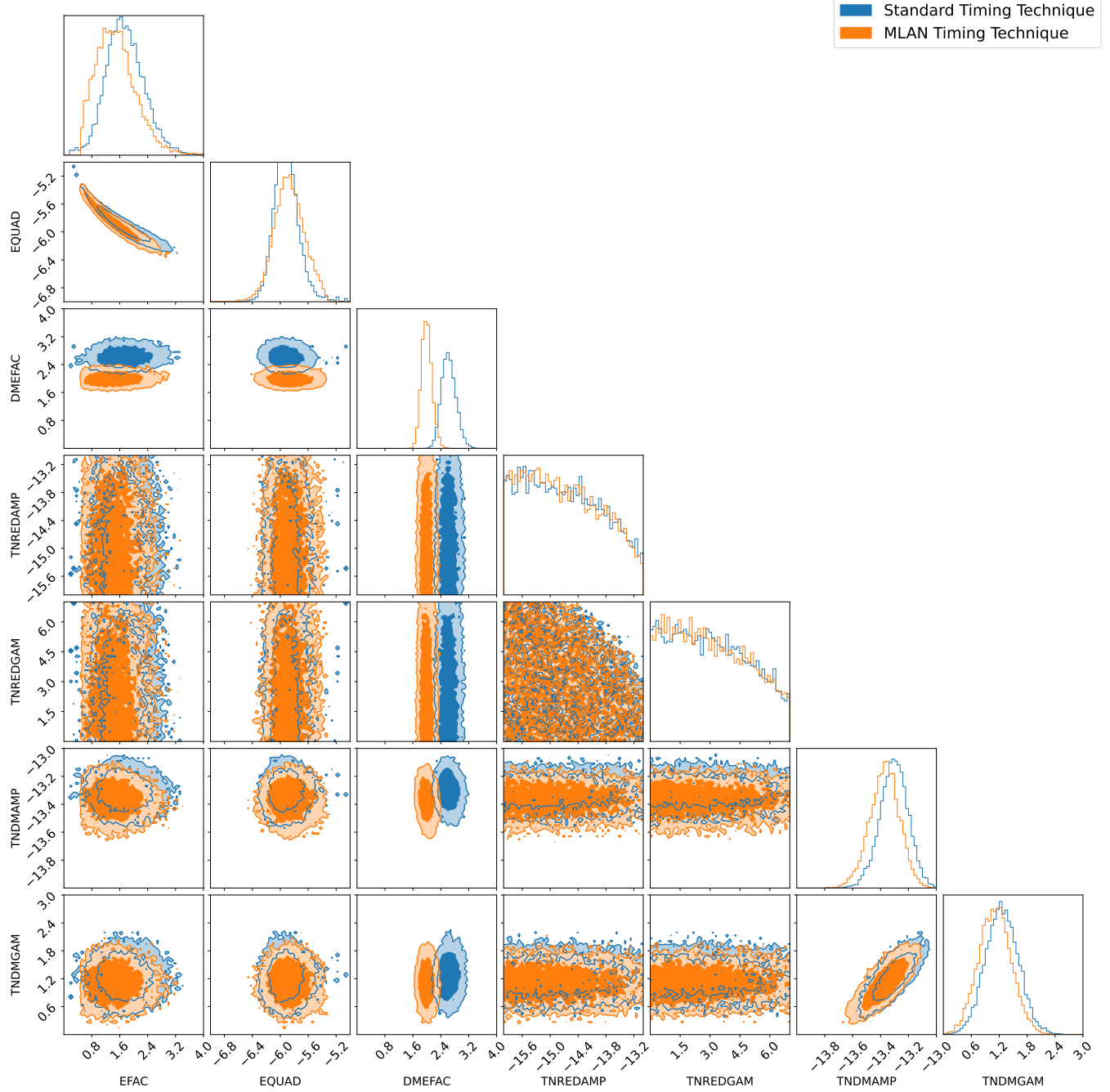


Figure 7. Corner plot showing the SPNA posterior distribution for PSR J2124-3358. The results for wideband measurements made using the standard and MLAN methods are displayed in different colors. The EQUAD and achromatic red noise parameter estimates are consistent between the standard and MLAN methods. On the other hand, the EFAC, DMEFAC, and DM noise estimates are lower for the MLAN method. This indicates that the standard method underestimates the measurement uncertainties, whereas the MLAN method provides more realistic measurement uncertainty estimates.

Nobleson K., et al., 2022, *Monthly Notices of the Royal Astronomical Society*, **512**, 1234
 Paladi A. K., Dwivedi C., Rana P., Nobleson K., Susobhanan A., et al., 2024, *MNRAS*, **527**, 213
 Pennucci T. T., 2019, *The Astrophysical Journal*, 871, 34
 Pennucci T. T., Demorest P. B., Ransom S. M., 2014, *The Astrophysical Journal*, **790**, 93
 Rana P., et al., 2025, *Publ. Astron. Soc. Australia*, **42**, e108
 Rickett B. J., 1970, *Monthly Notices of the Royal Astronomical Society*, 150,

67
 Susobhanan A., 2025, *Physical Review D*, **112**, 063023
 Susobhanan A., van Haasteren R., 2025, *MNRAS*, **542**, 2892
 Susobhanan A., et al., 2021, *Publ. Astron. Soc. Australia*, **38**, e017
 Susobhanan A., Kaplan D. L., Archibald A. M., Luo J., Ray P. S., et al., 2024, *The Astrophysical Journal*, 971, 150
 Tarafdar P., Nobleson K., Rana P., Singha J., Krishnakumar M. A., et al., 2022, *Publications of the Astronomical Society of Australia*, **39**, e053
 Taylor J. H., 1992, *Philosophical Transactions of the Royal Society of London*.

Series A: Physical and Engineering Sciences, 341, 117

Virtanen P., et al., 2020, *Nature Medicine*, 17, 261

van Haasteren R., Vallisneri M., 2014, *Phys. Rev. D*, 90, 104012

APPENDIX A: DERIVATION OF THE AMPLITUDE AND NOISE-MARGINALIZED LIKELIHOOD FOR WIDEBAND MEASUREMENTS

We begin by recalling the posterior distribution given in equation 8:

$$\begin{aligned} p[\varphi_0, D, \mathbf{a}, \sigma | P, T] &= L[P | \varphi_0, D, \mathbf{a}, \sigma; T] \\ &\propto \Pi[\varphi_0] \Pi[D] \Pi[\mathbf{a}] \Pi[\sigma] / Z[P | T], \end{aligned}$$

where the likelihood function is given by equation 6:

$$\ln L = - \sum_{\alpha=1}^{N_{\text{chan}}} \left[\sigma_{\alpha}^{-2} \left(U_{\alpha} + a_{\alpha}^2 V_{\alpha} - 2a_{\alpha} W_{\alpha} \right) + \frac{N_{\text{bin}}}{2} \ln [\pi \sigma_{\alpha}^2] \right].$$

Assuming an improper uniform prior $\Pi[a_{\alpha}] \propto 1$ and marginalizing, we obtain

$$\begin{aligned} p[\varphi_0, D, \sigma | P, T] &\propto \Pi[\varphi_0] \Pi[D] \Pi[\sigma] \int d^{N_{\text{chan}}} \mathbf{a} L[P | \varphi_0, D, \mathbf{a}, \sigma] \\ &= \Pi[\varphi_0] \Pi[D] \Pi[\sigma] L[P | \varphi_0, D, \sigma], \end{aligned} \quad (\text{A1})$$

where the amplitude-marginalized likelihood can be obtained by completing the square in equation (6) for a_{α} and evaluating the Gaussian integral. This gives

$$\begin{aligned} L[P | \varphi_0, D, \sigma_{\alpha}] &= \prod_{\alpha=1}^{N_{\text{chan}}} \frac{1}{(\sqrt{\pi} \sigma_{\alpha})^{N_{\text{bin}}-1} \sqrt{V_{\alpha}}} \\ &\times \exp \left\{ -\sigma_{\alpha}^{-2} \left(U_{\alpha} - V_{\alpha}^{-1} W_{\alpha}^2 \right) \right\}. \end{aligned} \quad (\text{A2})$$

$p[\varphi_0, D, \sigma | P, T]$ can be analytically marginalized over σ by assuming an improper log-uniform prior such that $\Pi[\sigma_{\alpha}] \propto \sigma_{\alpha}^{-1}$; i.e.,

$$\begin{aligned} p[\varphi_0, D | P, T] &\propto \Pi[\varphi_0] \Pi[D] \int d^{N_{\text{chan}}} \sigma L[P | \varphi_0, D, \mathbf{a}, \sigma] \Pi[\sigma] \\ &= \Pi[\varphi_0] \Pi[D] L[P | \varphi_0, D], \end{aligned} \quad (\text{A3})$$

where the marginalized likelihood can be obtained with the help of the inverse-gamma distribution to be

$$L[P | \varphi_0, D] = \prod_{\alpha=1}^{N_{\text{chan}}} \frac{\Gamma \left[\frac{N_{\text{bin}}-1}{2} \right]}{2 \sqrt{\pi^{N_{\text{bin}}-1} V_{\alpha}}} \left(U_{\alpha} - V_{\alpha}^{-1} W_{\alpha}^2 \right)^{\frac{1-N_{\text{bin}}}{2}}. \quad (\text{A4})$$

Dropping the factors that are independent of the parameters of interest φ_0 and D , we can write the marginalized log-likelihood as

$$\ln \Lambda = \frac{-(N_{\text{bin}}-1)}{2} \sum_{\alpha} \ln \left(U_{\alpha} - \frac{W_{\alpha}^2}{V_{\alpha}} \right), \quad (\text{A5})$$

which is a function of only the parameters of interest, φ_0 and D , as well as ν_{ref} .

APPENDIX B: DERIVATION OF THE AMPLITUDE AND NOISE-MAXIMIZED LIKELIHOOD FOR WIDEBAND MEASUREMENTS

Following Pennucci et al. (2014), we maximize equation (6) with respect to the a_{α} parameters, and this yields

$$\hat{a}_{\alpha} = W_{\alpha} / V_{\alpha}. \quad (\text{B1})$$

Substituting, we obtain

$$\ln L \Big|_{\hat{a}_{\alpha}} = - \sum_{\alpha=1}^{N_{\text{chan}}} \left[\sigma_{\alpha}^{-2} \left(U_{\alpha} - \frac{W_{\alpha}^2}{V_{\alpha}} \right) + \frac{N_{\text{bin}}}{2} \ln \sigma_{\alpha}^2 \right]. \quad (\text{B2})$$

We now maximize this expression over the σ_{α} parameters:

$$\hat{\sigma}_{\alpha}^2 = 2N_{\text{bin}}^{-1} \left(U_{\alpha} - \frac{W_{\alpha}^2}{V_{\alpha}} \right). \quad (\text{B3})$$

Substituting this in equation (B2) and discarding additive constant terms, we obtain

$$\ln \hat{L} = \ln L \Big|_{\hat{a}_{\alpha}, \hat{\sigma}_{\alpha}} = \frac{-N_{\text{bin}}}{2} \sum_{\alpha} \ln \left(U_{\alpha} - \frac{W_{\alpha}^2}{V_{\alpha}} \right), \quad (\text{B4})$$

APPENDIX C: DERIVATION OF THE FIDUCIAL FREQUENCY AND THE MEASUREMENT UNCERTAINTIES

When the signal-to-noise ratio in the observed portrait P is large, we expect the distribution of φ_0 and D to be approximately Gaussian. Under this assumption, the measurement covariance matrix Ξ of φ_0 and D can be approximated as $\Xi = -\mathbf{H}^{-1}$, where

$$\mathbf{H} = \begin{bmatrix} \frac{\partial^2 \ln \Lambda}{\partial \varphi_0^2} & \frac{\partial^2 \ln \Lambda}{\partial \varphi_0 \partial D} \\ \frac{\partial^2 \ln \Lambda}{\partial \varphi_0 \partial D} & \frac{\partial^2 \ln \Lambda}{\partial D^2} \end{bmatrix} \quad (\text{C1})$$

is the Hessian of $\ln \Lambda$.

The measurement covariance can be made to vanish by choosing a value of ν_{ref} such that $\frac{\partial^2 \ln \Lambda}{\partial \varphi_0 \partial D} = 0$. We begin by differentiating equation (2) by φ_0 and D :

$$\frac{\partial \varphi_{\alpha}}{\partial \varphi_0} = 1, \quad (\text{C2a})$$

$$\frac{\partial \varphi_{\alpha}}{\partial D} = \kappa \bar{F} \left(\nu_{\alpha}^{-2} - \nu_{\text{ref}}^{-2} \right). \quad (\text{C2b})$$

Differentiating equation (B4), we obtain

$$\frac{\partial \log \Lambda}{\partial \varphi_{\alpha}} = (N_{\text{bin}} - 1) \frac{W_{\alpha} W'_{\alpha}}{(U_{\alpha} V_{\alpha} - W_{\alpha}^2)}, \quad (\text{C3a})$$

$$\frac{\partial^2 \log \Lambda}{\partial \varphi_{\alpha} \partial \varphi_{\beta}} = \delta_{\alpha\beta} (N_{\text{bin}} - 1) \quad (\text{C3b})$$

$$\times \frac{(W'_{\alpha}^2 (U_{\alpha} V_{\alpha} + W_{\alpha}^2) + W_{\alpha} W''_{\alpha} (U_{\alpha} V_{\alpha} - W_{\alpha}^2))}{(U_{\alpha} V_{\alpha} - W_{\alpha}^2)^2}, \quad (\text{C3c})$$

where, from equation (7c), we can derive

$$W'_{\alpha} = \frac{\partial W_{\alpha}}{\partial \varphi_{\alpha}} = -2\pi \sum_{k=1}^{N_{\text{bin}}/2} k \Im \left[\tilde{P}_{\alpha k} \tilde{T}_{\alpha k}^* \exp[2\pi i k \varphi_{\alpha}] \right], \quad (\text{C4a})$$

$$W''_{\alpha} = \frac{\partial^2 W_{\alpha}}{\partial \varphi_{\alpha}^2} = -4\pi^2 \sum_{k=1}^{N_{\text{bin}}/2} k^2 \Re \left[\tilde{P}_{\alpha k} \tilde{T}_{\alpha k}^* \exp[2\pi i k \varphi_{\alpha}] \right]. \quad (\text{C4b})$$

It is easy to show from the above expressions that

$$\frac{\partial^2 \ln \Lambda}{\partial D \partial \varphi_0} = \kappa \bar{F} \sum_{\alpha} \frac{\partial^2 \ln \Lambda}{\partial \varphi_{\alpha}^2} \left(\nu_{\alpha}^{-2} - \nu_{\text{ref}}^{-2} \right). \quad (\text{C5})$$

Setting this derivative to zero, we obtain

$$\bar{\nu}_{\text{ref}}^2 = \frac{\sum_{\alpha} \frac{\partial^2 \ln \Lambda}{\partial \varphi_{\alpha}^2}}{\sum_{\alpha} \frac{\partial^2 \ln \Lambda}{\partial \varphi_{\alpha}^2} \nu_{\alpha}^{-2}}. \quad (\text{C6})$$

Note that the right-hand side of the above equation is a function of φ_0 , D , and ν_{ref} . In practice, we compute $\bar{\nu}_{\text{ref}}$ by first estimating φ_0 and D using an arbitrary value of ν_{ref} , and then evaluating equation (C6) using those estimated values.

With this choice of ν_{ref} , the measurement variances in φ_0 and D can be estimated as

$$\sigma_{\varphi_0}^2 = - \left(\frac{\partial^2 \ln \Lambda}{\partial \varphi_0^2} \right)^{-1} = - \left(\sum_{\alpha} \frac{\partial^2 \ln \Lambda}{\partial \varphi_{\alpha}^2} \right)^{-1}, \quad (\text{C7a})$$

$$\sigma_D^2 = - \left(\frac{\partial^2 \ln \Lambda}{\partial D^2} \right)^{-1} = - \left(\kappa^2 \bar{F}^2 \sum_{\alpha} \frac{\partial^2 \ln \Lambda}{\partial \varphi_{\alpha}^2} \left(\nu_{\alpha}^{-2} - \nu_{\text{ref}}^{-2} \right)^2 \right)^{-1}, \quad (\text{C7b})$$

and the TOA variance is

$$\sigma_{t_{\text{arr}}}^2 = \bar{F}^{-2} \sigma_{\varphi_0}^2. \quad (\text{C8})$$

Since $\ln \Lambda$ and $\ln \hat{L}$ have similar functional forms, the ν_{ref} and uncertainty computations given above can be easily repeated for $\ln \hat{L}$. It is easy to show that the parameter variances estimated from $\ln \Lambda$ are $\frac{N_{\text{bin}}}{N_{\text{bin}} - 1}$ times the variances estimated from $\ln \hat{L}$, and hence slightly more conservative. This difference becomes negligible for large values of N_{bin} .

This paper has been typeset from a $\text{TeX}/\text{\LaTeX}$ file prepared by the author.